Sheffield Hallam University

In situ poling X-ray diffraction studies of lead-free BiFeO3–SrTiO3 ceramics

LU, Zhilun <http://orcid.org/0000-0002-9967-5221>, WANG, Ge, LI, Linhao, HUANG, Yuhe, FETEIRA, Antonio <http://orcid.org/0000-0001-8151-7009>, BAO, Weichao, KLEPPE, Annette K. <http://orcid.org/0000-0002-0258-3241>, XU, Fangfang, WANG, Dawei and REANEY, Ian M.

Available from Sheffield Hallam University Research Archive (SHURA) at:

http://shura.shu.ac.uk/28652/

Published version

Copyright and re-use policy

In situ poling X-ray diffraction studies of lead-free BiFeO₃–SrTiO₃ ceramics

Zhilun Lu [a, b, 1, *], Ge Wang [a, 1], Linhao Li [a], Yuhe Huang [a], Antonio Feteira [c], Weichao Bao [d], Annette K. Kleppe [e], Fangfang Xu [d], Dawei Wang [a, f, **], Ian M. Reaney [a, ***]

[a] Department of Materials Science and Engineering, University of Sheffield, Sheffield, S1 3JD, UK
[b] The Henry Royce Institute, Sir Robert Hadfield Building, Sheffield, S1 3JD, UK
[c] Materials and Engineering Research Institute, Sheffield Hallam University, Sheffield, S1 1WB, UK
[d] State Key Laboratory of High Performance Ceramics and Superfine Microstructure, Shanghai Institute of Ceramics, Shanghai, 200050, China
[e] Diamond Light Source Ltd, Harwell Science and Innovation Campus, Didcot, OX11 0DE, UK
[f] Shenzhen Institute of Advanced Electronic Materials, Shenzhen Institute of Advanced Technology, Chinese Academy of Sciences, Shenzhen, 518055, China

ABSTRACT

The origin of the large electrostrain in BiFeO₃-BaTiO₃ (BF-BT) ceramics is controversial and has been attributed to either a field-induced transition to a long-range ferroelectric (FE) state or to multi-symmetry, polar nanoregions within a pseudocubic matrix whose vectors approximately align with the direction of the applied field. The $(1-x)$BiFeO₃-xSrTiO₃ (BF-xST) solid solution is structurally and microstructurally similar to BF-BT and provides a further case study to assess the origin of electrostrain. In BF-xST, electrostrain is optimized at $x = 0.4$ (0.15%) which zero field, room temperature full-pattern X-ray diffraction (XRD) Rietveld refinement and scanning/transmission electron microscopy suggest is composed of 15% rhombohedral (R) cores, surrounded by 85% pseudocubic (PC) shells. In-situ poling synchrotron XRD reveals that all peaks remain singlet and exhibit no change in full width half maximum up to 100 kV cm⁻¹, confirming the absence of long-range FE order and the retention of short-range polar order, despite the large applied field. Strain anisotropy (calculated from individual peaks) of $\varepsilon_{220} > \varepsilon_{111} > \varepsilon_{200}$ and the associated strain orientation distribution however, indicate the existence of local orthorhombic (O), R and tetragonal (T) symmetries. The data therefore imply the existence under poling of multi-symmetry polar nanoregions in BF-0.4ST rather than a long FE phase, supporting the model described by Wang and co-workers (2019) for BF-BT compositions.

© 2021 The Author(s). Published by Elsevier Ltd. This is an open access article under the CC BY license (http://creativecommons.org/licenses/by/4.0/).

1. Introduction

BiFeO₃ (BF) ceramics possess a large polarization of 90–100 μC cm⁻² and a very high ferroelectric (FE) Curie temperature (T$_C$) of 1093 K [1,2]. However, the difficulty of fabricating single phase BF ceramics has limited material characterization and device applications, leading to most attention being focused on BF-based solid solutions [3–6]. One of the most promising examples is (1-x)BiFeO₃-xBaTiO₃ (BF-xBT). Although often reported as having a morphotropic phase boundary (MPB) between BF-rich rhombohedral (R) phase and BT-rich tetragonal (T) phase, properties are optimized within a diffuse mixed phase region consisting of R and pseudocubic (PC) phases at $0.25 < x < 0.35$, where high FE T$_C$, large maximum and remanent polarizations (P$_{max}$ and P$_r$), and excellent piezoelectric coefficients (d_{33}) and electric field-induced strain (electrostrain) [7–10] have been reported. Compared to other lead-free piezoelectrics, e.g. Na$_{0.5}$Bi$_{0.5}$TiO₃ (NBT)-based materials, BF based materials have a more complex, core-shell structure. The formation of a core-shell structure, the core/shell volume ratio and their composition can potentially affect the electrical properties. Quenching has proved an effective method to modify the core-shell structure and therefore, electrical properties [11].

* Corresponding author. Department of Materials Science and Engineering, University of Sheffield, Sheffield, S1 3JD, UK.
** Corresponding author. Shenzhen Institute of Advanced Electronic Materials, Shenzhen Institute of Advanced Technology, Chinese Academy of Sciences, Shenzhen, 518055, China.
*** Corresponding author. Department of Materials Science and Engineering, University of Sheffield, Sheffield, S1 3JD, UK.
E-mail addresses: zhilun.lu@sheffield.ac.uk (Z. Lu), wangdawei102@gmail.com (D. Wang), i.m.reaney@sheffield.ac.uk (I.M. Reaney).
1 Zhilun Lu and Ge Wang contributed equally to this work.

BF-BT however, suffers from volatilization of Bi and the formation of mixed valence Fe ions during sintering [12,13], leading to high levels of conductivity, particularly at elevated temperatures (>100 °C). This has driven extensive investigations into the role of A-site (e.g. La and Nd) [14–16] and/or B-site stoichiometric dopants (e.g. Al, Co, Ga, $Ni_{1/2}Ti_{1/2}$, $Mg_{1/2}Ti_{1/2}$) [17–23] on electrical resistivity and piezoelectric properties of BF-BT ceramics. Aliovalent doping has also been investigated and electrical conductivity of BF-based materials is suppressed by Nb and Mn [24–29], with excellent electrostrain (S_{max} > 0.4%, strain coefficient d_{33}^* > 500 pm V^{-1}) reported in BF-BT-based solid solutions with 0.1%–0.5% excess Mn, e.g. BF-BT-Nd, BF-BT-$Bi(Mg_{2/3}Nb_{1/3})O_3$ and BF-BT-$Bi(Zn_{2/3}Nb_{1/3})O_3$ [16,21,30].

Despite extensive studies of BF-BT-based solid solutions, the origin of the excellent electrostrain for BF-BT-based materials remains controversial. Chen and co-workers [31] reported a high electrostrain of 0.38% at 60 kV cm^{-1} for 0.64BF-0.36BT ceramics due to a combination of lattice distortion, domain switching and a field-induced phase transition. Wada and co-workers proposed that the origin of electrostrain in BF-BT-$0.1Bi(Mg_{1/2}Ti_{1/2})O_3$ ceramics was associated with off-centered Bi ion grain-to-grain interactions [32]. Wang, Reaney and co-workers reported electrostrain of ~0.6% in BF-BT-$0.01Nd(Li_{1/2}Nb_{1/2})O_3$ ceramics at 150 kV cm^{-1} under *in-situ* poling synchrotron X-ray diffraction (XRD) [33]. Prior, during and after application of electric field, the structure remained *PC* without any change in full width half maximum (FWHM) of XRD peaks. Instead, strain anisotropy of XRD peaks (ε_{200} > ε_{220} > ε_{111}) indicated the presence of multi-symmetry polar nanoregions, which permitted a large average distortion in the direction of the applied field. Similar characterization and strain behavior were also reported in BF-BT-$BiScO_3$ and BF-BT-$Bi(Mg_{2/3}Nb_{1/3})O_3$ [33]. In contrast to BF-BT [19,32,34–36], there is a consensus that the origin of the large electrostrain in NBT based materials results from a field-induced transition from a short to a long range ordered state [37–41]. The wider understanding of electrostrain in polar materials would therefore, benefit from further in-depth studies of BF-based systems.

$BiFeO_3$-$SrTiO_3$ (BF-ST) is a promising candidate to investigate further the origin of electrostrain in BF-based materials but most studies to date have focussed on magnetic [42–45] rather than FE and piezoelectric properties, because of its high leakage current [43] and high coercive field (E_c) compared to BF-BT. However, BF-ST ceramics were recently doped with donor Nb-ions (1–3 mol%) which suppressed the high leakage current, resulting in large breakdown strength at room temperature [46]. Therefore, these modified BF-ST compositions are suitable to not only evaluate electrical, FE and piezoelectric properties but also to undertake *in-situ* synchrotron studies under large applied fields.

In this work, the detailed phase structure, dielectric, FE and piezoelectric properties of Nb-doped (1-*x*)BF-*x*ST (*x* = 0.1–0.5) ceramics are investigated with optimized electrical and piezoelectric properties obtained at *x* = 0.4 within a mixed *R* and *PC* region, in which a small volume core of *R* phase is surrounded by a large volume of *PC* shell regions. *In-situ* poling synchrotron XRD is employed for the first-time in BF-ST ceramics to rationalise the origin of the optimized electrostrain for *x* = 0.4. Under electric field, the average structure of *x* = 0.4 remains *PC* (singlet XRD reflections) but exhibits strain anisotropy with ε_{220} > ε_{111} > ε_{200}, confirming the absence of electric field-induced long-range order and supporting the "multi-symmetry polar nanoregion" model, described by Wang and co-workers [33].

2. Methods

(1-*x*)BF-*x*ST-0.01Nb (*x* = 0.1, 0.2, 0.3, 0.4 and 0.5) ceramics were prepared using analytical-grade Bi_2O_3, Fe_2O_3, $SrCO_3$, TiO_2 and Nb_2O_5 by a solid state reaction method. Stoichiometric amounts of dried raw powders were weighed and ball-milled 12 h in isopropanol using Y_2O_3-stabilized ZrO_2 as grinding media. The mixed powders were dried, calcined 2 h at 800 °C and then ball milled 12 h. After uniaxially pressing, ceramic samples were sintered 3 h at 1030–1150 °C. The densities of the sintered ceramics were measured using the Archimedes method. Surfaces of sintered ceramics were ground, and gold paste electrodes applied. Impedance spectroscopy (IS) data was obtained by an Agilent E4980A (Agilent Technologies Inc., Palo-Alto, CA) from 20 Hz to 1 MHz at 100 mV. Electrical conductivity was obtained by fitting the experimental data using ZView software (Scribner Associates, Inc., Southern Pines, NC). Temperature dependence of dielectric properties were measured using an Agilent 4184A precision LCR meter from room temperature to 550 °C at 10, 100, 250 kHz and 1 MHz. IS and dielectric data were corrected by a geometric factor (thickness/ surface area). Bipolar polarisation-electric field (*P-E*) and strain-electric field (*S-E*) loops were obtained using an aixACCT TF 2000E FE tester at 1Hz. The polished surface of the ceramic samples was observed using an FEI Inspect F50 scanning electron microscope (SEM) with backscattered electron (BSE) and energy-dispersive spectroscopy (EDS) detectors. Transmission electron microscopy (TEM) data were obtained using a JEOL JEM 2100F (JEOL, Tokyo, Japan) operated at 200 kV.

To evaluate the electrostrain of (1-*x*)BF-*x*ST ceramics, *in-situ* poling synchrotron XRD was employed, as schematically shown in Fig. 1. *In-situ* poling synchrotron XRD experiments were performed at the I15 Diamond light source with a photon energy of 72 keV (0.1722 Å). Ceramic samples were cut into bars (L5 × W1 × T0.2 mm) and annealed 2 h at 800 °C to eliminate residual stresses. During *in-situ* experiments, the bar-shaped samples were polished down to 0.2 mm thickness and placed in a custom-designed polyimide holder with silicone oil. The sample holder was electrically connected with a high voltage amplifier (Matsusada EC-10). The X-ray beam was focused and collimated to 70 μm diameter. Transmission and two-dimensional (2D) diffraction patterns were collected simultaneously under electric field up to 100 kV cm^{-1} with 12.5 kV cm^{-1} intervals using Pilatus 2 M detector located approximately 1 m downstream of the sample and converted every 15° into conventional one-dimensional (1D) XRD patterns with intersection angle (ψ) to the direction of the electric field [33]. XRD patterns of ψ = 0° and ψ = 90° correspond to the direction parallel and perpendicular to the applied electric field,
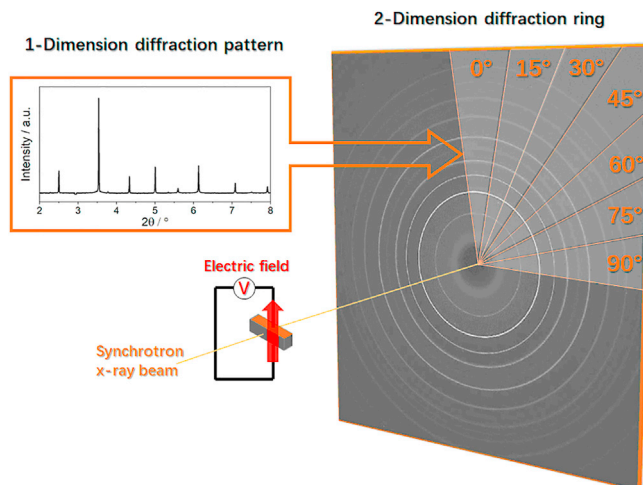

Fig. 1. The schematic of the setup of the *in-situ* poling synchrotron XRD experiment.

respectively. Peak fitting was conducted in TOPAS using a pseudo-Voigt function with crystallographic information of the ceramic obtained from full-pattern Rietveld refinements.

3. Results and discussions

3.1. Phase structure

The full-pattern Rietveld refinement results of $(1-x)$BF-xST ($x = 0.1, 0.2, 0.3, 0.4$ and 0.5) ceramics obtained at room temperature and zero field are presented in Fig. 2 and Table 1. The XRD full-pattern is refined using several single or mixed-phase models, such as the R (R3m/R3c), T (P4mm) and cubic (C, Pm$\overline{3}$m). Lattice parameters for each phase are fitted with fixed background, instruments information and peak type to obtain the phase fraction,

cell volume and refined parameters. At the highest BF concentration, $x = 0.1$, only R (R3c) phase is observed while for low BF concentrations ($x = 0.5$), XRD pattern is best fitted with single C (Pm$\overline{3}$m) phase. For $0.2 \leq x \leq 0.4$, XRD patterns is well refined with mixed R3c and Pm$\overline{3}$m phases, as evident by fitting of the $\{111\}_p$ and $\{200\}_p$ XRD representative peaks in Fig. 2a. The XRD full-pattern for $x = 0.4$ is best refined with 85% C and 15% R phases, consistent with previous reports [44].

4. Dielectric, ferroelectric and piezoelectric properties

The temperature-dependent dielectric permittivity (ε_r *vs. T*) and loss ($tan\delta$ *vs. T*) data of $(1-x)$BF-xST ($x = 0.1, 0.2, 0.3, 0.4$ and 0.5) ceramics are shown in Fig. 3. The broad ε_r peaks for $x = 0.1$ and 0.2 have been previously proposed to relate to the onset of
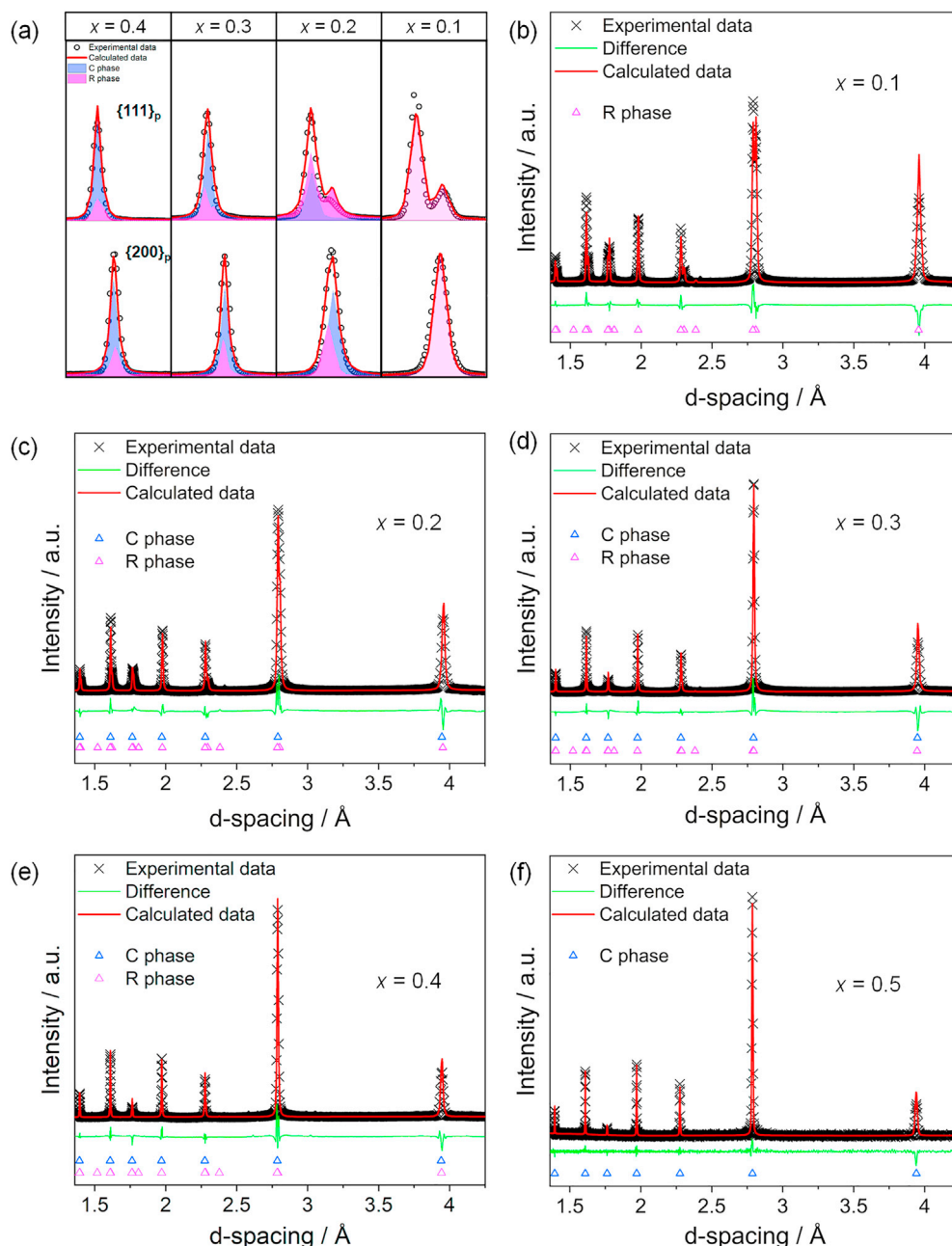

Fig. 2. Synchrotron XRD pattern and corresponding Rietveld refinement results for $(1-x)$BF-xST ceramics at room temperature.

Table 1
Summary of XRD Rietveld refinement results for (1-*x*)BF-*x*ST ceramics.

x	GOF	R_{exp}	R_{wp}	C phase-Pm$\overline{3}$m			R phase-R3c			
				Phase fraction	Cell volume (Å³)	Lattice *a* (Å)	Phase fraction	Cell volume (Å³)	Lattice *a* (Å)	Lattice *c* (Å)
0.1	1.06	11.06	11.88	0%	N/A	N/A	100%	371.94(3)	5.5766(2)	13.8104(6)
0.2	1.08	11.11	11.98	30%	61.445(11)	3.9460(2)	70%	370.52(6)	5.5731(4)	13.7746(10)
0.3	1.07	13.2	14.17	74%	61.569(5)	3.94871(11)	26%	368.95(9)	5.5749(5)	13.7080(19)
0.4	1.08	11.56	12.48	85%	61.189(5)	3.94056(7)	15%	367.75(15)	5.5706(9)	13.684(3)
0.5	1.12	10.67	11.95	100%	61.23(3)	3.9415(7)	0%	N/A	N/A	N/A

GOF: goodness of fitting.

ferroelectricity or the existence of a relaxor/FE phase [6] but there is no evidence of Curie-Weiss behavior. There is some frequency dispersion within the ε_r *vs. T* plots for *x* = 0.1 and 0.2 but the high *tanδ* above 300 °C casts doubt as to whether these maxima can be ascribed to relaxor behavior. Compositions with 0.3 ≤ *x* ≤ 0.5 however, have well-defined broad Curie maxima (T_m) which decrease in temperature with increasing ST concentration. We propose that any phase transitions (T_m) for *x* = 0.1 and 0.2 are above 500 °C and are not recorded in the data. Even if higher temperature data are available, the high conductivity would likely obscure changes in the ε_r *vs. T* that relate to the onset of FE/relaxor behavior. With increasing ST concentration, T_m decreases and becomes visible in ε_r *vs. T* plots below 500 °C for 0.3 ≤ *x* ≤ 0.5. Irrespective of the interpretation, all ε_r *vs. T* plots are consistent with previously published data [6] with the broad peaks for 0.3 ≤ *x* ≤ 0.5 presumably arising from a combination of the FE *R* core and the relaxor *PC* shell within grains.

Room temperature *P-E* and *S-E* loops of (1-*x*)BF-*x*ST (*x* = 0.1, 0.2, 0.3, 0.4 and 0.5) ceramics at an electric field of 150 kV cm⁻¹ are presented in Fig. 4. Compositions with *x* = 0.1 and 0.2 exhibit behavior consistent with a 'lossy' linear dielectric, often associated with BF-rich compositions [47,48]. We propose that the high

transition temperature (>500 °C), implied from the ε_r *vs. T* data in Fig. 2, may inhibit FE switching with opening of the loop only related to polarization from space-charge regions. The *P-E* and *S-E* loops for *x* = 0.3 and 0.4 exhibit FE hysteresis with the largest P_r~45.5 μC cm⁻², E_c~86 kV cm⁻¹ and S_{max}~0.09% for *x* = 0.3 [49]. These compositions also have small negative strains in the *S-E* loops, suggesting at least, in part, a contribution from FE behavior (*R* phase) to the strain but which diminishes at *x* = 0.5. Optimized electromechanical properties, P_{max} of 52.7 μC cm⁻² and S_{max} of 0.15% are observed for *x* = 0.4. The *P-E* for *x* = 0.5 becomes significantly slimmer with an absence of negative strain in the *S-E*, exhibiting a typical relaxor behavior. A combination of XRD refinements, ε_r *vs. T* and *P/S−E* plots therefore, suggests a transition from a FE to relaxor state as a function of increasing *x*. The trend is identical to that observed for BF-BT compositions by several authors [8,50].

5. Microstructure for *x* = 0.4

Backscattered Electron (BSE) images of the polished surface for *x* = 0.4 ceramic are presented in Fig. 5a. Ceramics exhibit polygonal grains with an average ~2 μm diameter and minimal porosity
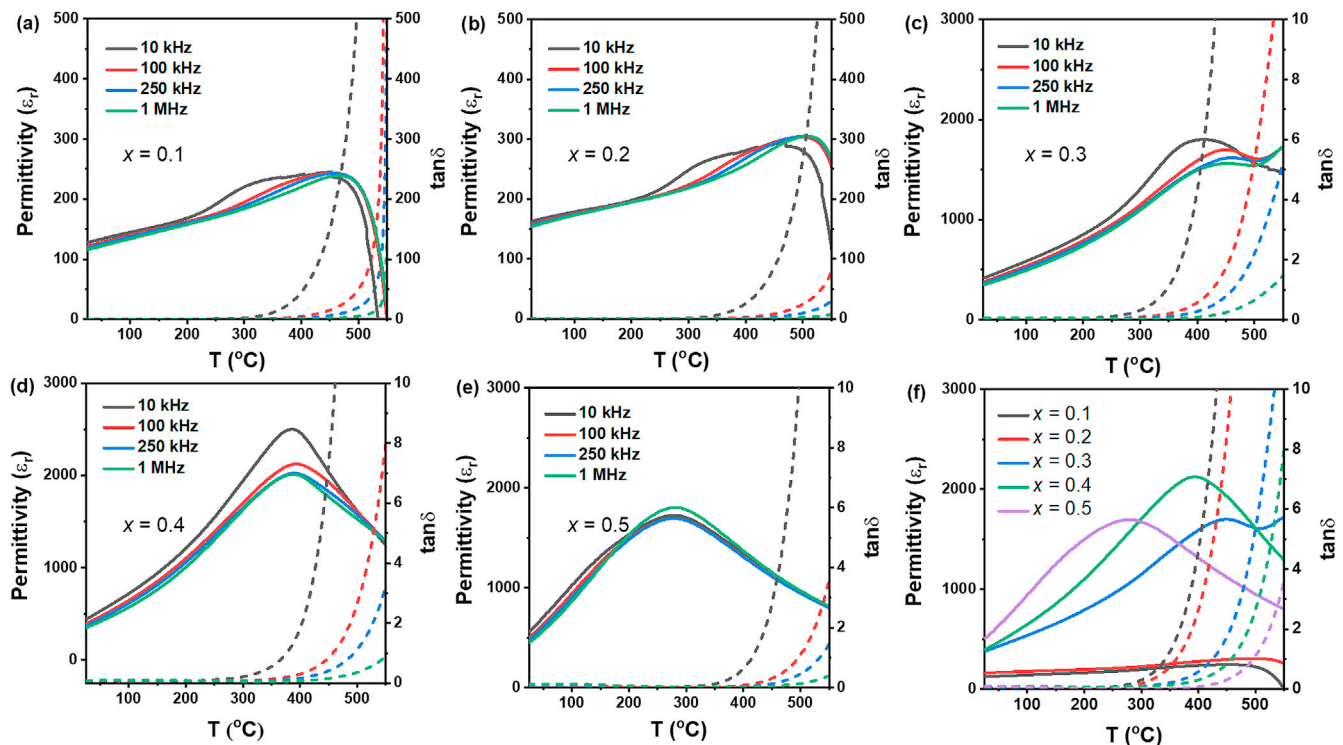

Fig. 3. (a) The temperature dependence of dielectric permittivity (ε_r *vs. T*) and loss (*tanδ vs. T*) of (1-*x*)BF-*x*ST ceramics, (a) *x* = 0.1, (b) *x* = 0.2, (c) *x* = 0.3, (d) *x* = 0.4, (e) *x* = 0.5 and (f) The temperature dependence of ε_r and *tanδ* compared at 100k Hz.
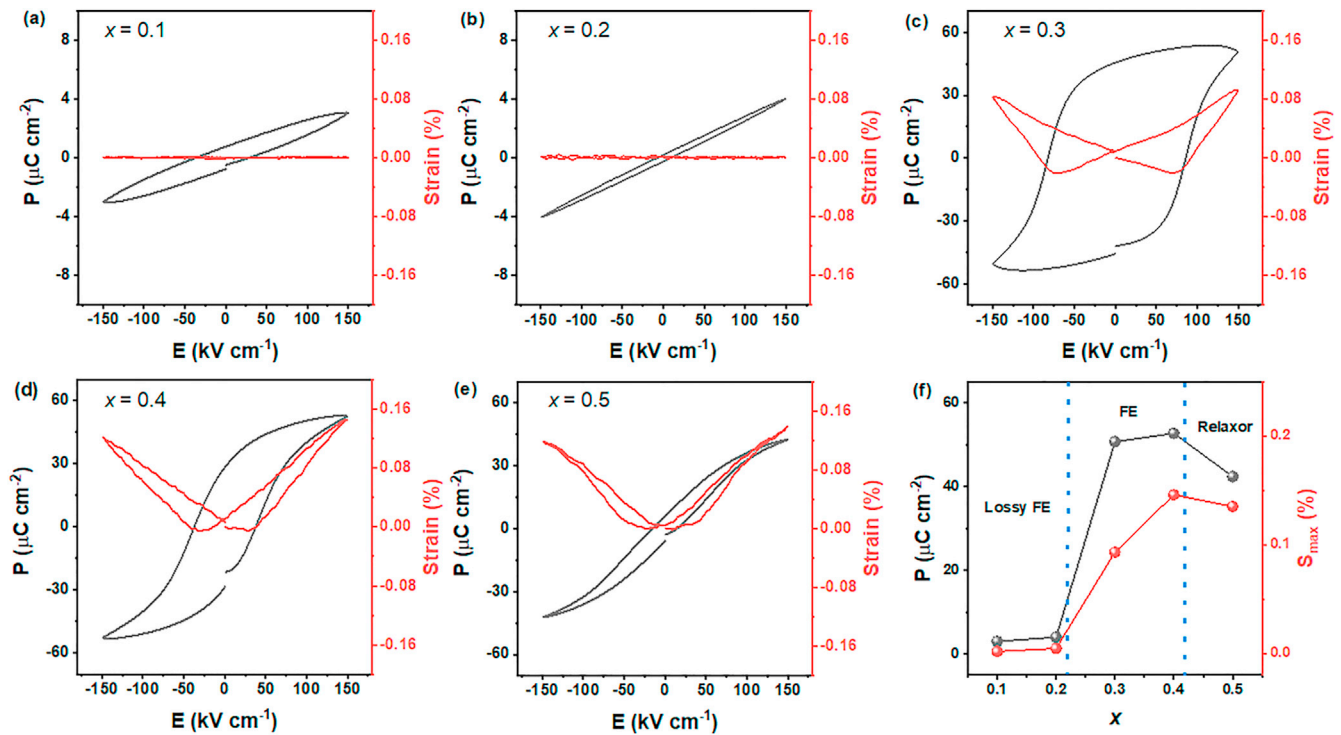
Fig. 4. Room temperature P-E and S-E loops under 150 kV cm^{-1} of $(1-x)$BF-xST ceramics, (a) $x = 0.1$, (b) $x = 0.2$, (c) $x = 0.3$, (d) $x = 0.4$ and (e) $x = 0.5$. (f) Variation of P_{max} and S_{max} as function of x.

(relative density > 95%). Core-shell regions are observed, with most grains displaying bright cores (Bi/Fe rich) and dark shells (Sr/Ti rich). The detailed quantitative data for each microstructural feature are shown in Table 2. We propose that the C phase from XRD refinements is Sr/Ti rich and resides within the shell and the R phase is Bi/Fe rich within the core. A core-shell microstructure is associated with immiscibility on cooling from the sintering temperature that leads to microchemical segregation, commonly observed in BF-based ceramic systems [33,46]. TEM images reveal the presence of a meso-domain structure within the grain core as displayed in Fig. 5b, consistent with a FE R phase with minimum diffraction contrast in the PC shell regions.

6. *In-situ* poling synchrotron XRD for $x = 0.4$

Synchrotron XRD patterns of ceramics with $x = 0.4$ are recorded

Table 2
Average atomic percentage (excl. O) calculated from EDS spectra obtained from different phases presented in $x = 0.4$.

Elements	Bright Core (mol%)	Dark Shell (mol%)
Bi	35.5	29.2
Fe	40.6	28.9
Sr	13.8	20.8
Ti	10.1	21.1

from an unpoled ($E = 0$ kV cm^{-1}) to poled ($E_{max} = 100$ kV cm^{-1}, beyond E_c) to unpoled ($E = 0$ kV cm^{-1}) state with a step size of 12.5 kV cm^{-1}. Contour surface plots (Fig. 6) show variations in the $\{111\}_p$, $\{200\}_p$ and $\{220\}_p$ peak profiles under a full cycle of bipolar electric field ($E_{max} = 100$ kV cm^{-1}) for $x = 0.4$ at $\psi = 0°$ and 90°, representing the longitudinal strains (positive) and transverse
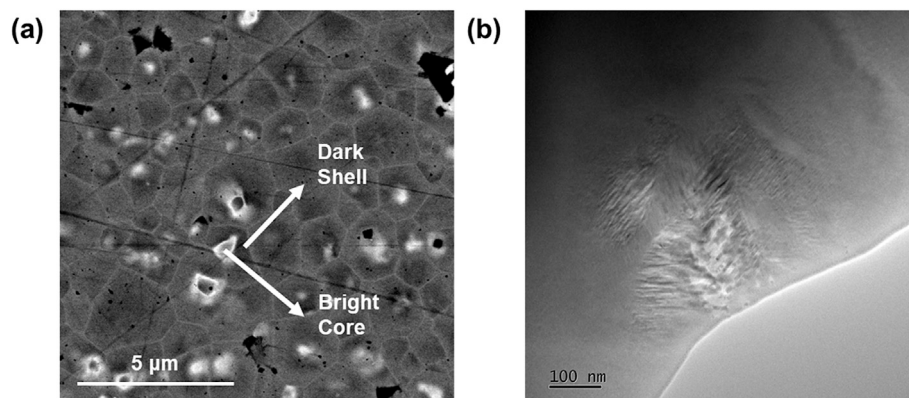

Fig. 5. (a) Backscattered Electron (BSE) image of the polished surface and (b) TEM bright field image.

strains (negative), respectively. Prior, during and after application of electric field of 100 kV cm^{-1}, {111}$_p$, {200}$_p$ and {220}$_p$ peaks remain singlet without splitting, suggesting no occurrence of macroscopic domain switching and phase transitions. Similar behavior was also reported in our previous work on BF-BT-based materials under an electric field of 150 kV cm^{-1} [33]. Fig. 6 confirms that BF-ST solid solutions are less prone to field-induced structural phase transition to a long-range FE state than other relaxor materials, such as La-doped lead zirconate titanate (PZT) and NBT-based materials [51,52].

With increasing electric field, {111}$_p$, {200}$_p$ and {220}$_p$ peaks shift to smaller 2θ angles at $\psi = 0°$, indicating increased d spacing and tensile stresses parallel to the direction of the electric field. In contrast, the peaks shift to higher angle at $\psi = 90°$, corresponding to compressive stress perpendicular to the electric field direction. The peak positions of initial unpoled state ($E = 0$ kV cm^{-1}), $+E_{max}$, 0, $-E_{max}$ and poled state ($E = 0$ kV cm^{-1}) are also plotted in Fig. 6, showing the variation of each single peak under application of electric field. There are no significant changes of FWHM in Fig. 7a, confirming again the absence of a macroscopic transition or changes in domain correlation [33]. More importantly, the peak position at the poled remanent state is slightly offset in comparison with the initial unpoled state, which will be further discussed in the later sections.

The electrostrain for lead-based and lead-free piezoelectrics is commonly contributed by a combination factors, i.e. structural transformation, domain switching and lattice strain, which can be calculated from XRD peaks, as reported by Jones [53,54] and Chen [55,56]. For compositions that remain PC phase during application of external electric field, the effective total electrostrain ($\varepsilon_{eff\ total}$) obtained from *in-situ* XRD poling experiment can also be simply estimated based on the weighted-average strain of individual {hkl} planes [57], as given by Eq. (1):

$$\varepsilon_{eff\ total} = \frac{\sum_{hkl} T_{hkl}(\psi) m_{hkl} \varepsilon_{hkl}(\psi)}{\sum_{hkl} T_{hkl}(\psi) m_{hkl}} \qquad (1)$$

where $T_{hkl}(\psi)$ is the domain texture index with angle ψ to the electric field, m_{hkl} is the multiplicity of {hkl} planes, and $\varepsilon_{hkl}(\psi)$ is the effective individual electrostrain with angle ψ to the electric field, which can be calculated from Eq. (2):

$$\varepsilon_{hkl}(\psi) = \frac{d_{hkl} - d_{hkl}^0}{d_{hkl}^0} \qquad (2)$$

Here, d_{hkl} and d_{hkl}^0 are the hkl interplanar spacings under electric field and without electric field, respectively. In the present case, $T_{hkl}(\psi) = 1$ due to the absence of crystallographic texture. The m_{hkl} values of {111}$_p$, {200}$_p$ and {220}$_p$ planes are 8, 6 and 12, respectively, according to a PC setting [58]. $\varepsilon_{hkl}(\psi)$ values are obtained from Eq. (2) through fitting of the {111}$_p$, {200}$_p$ and {220}$_p$ diffraction peaks from which the $\varepsilon_{eff\ total}$, may be estimated using Eq. (1).

The ε_{111}, ε_{200} and ε_{220} calculated from {111}$_p$, {200}$_p$ and {220}$_p$ peaks for $x = 0.4$ at $\psi = 0°$ and 90° up to a bipolar electric field of 100 kV cm^{-1} are shown in Fig. 7b. Positive and negative values are obtained in $\psi = 0°$ and 90°, indicating tensile and compressive strain, respectively. The highest strain under electric field of 100 kV cm^{-1} at $\psi = 0°$ for ε_{220}, ε_{111} and ε_{200} is +0.13%, +0.10% and +0.08%. Combined data of ε_{111}, ε_{200} and ε_{220}, Eq. (1) is employed to obtain the effective total electrostrain, as shown in Fig. 7c. The $\varepsilon_{eff\ total}$ are ~+0.11% at $\psi = 0°$ and −0.04% at $\psi = 90°$, which is close to that obtained from macroscopic S-E results (Fig. 4d).

Compared to BF-BT [33], a smaller electrostrain (<0.15%) is attained for BF-ST at higher fields (>100 kV cm^{-1}). The difference in response may be qualitatively related to the decrease in average cubo-octahedral and octahedral volumes in ST with respect to BT based solid solutions. Ba (1.64 Å) is a significantly larger ion than Sr (1.44 Å) [59] which would generally increase polarization and strain in solid solutions of the latter, in accordance with a simplistic 'rattling ion' model; i.e. the larger the average site volume, the greater the potential for displacement of the most polarizable species (Ti and Bi).

A contribution to strain from the FE R3c core (observed in SEM and TEM images) which would be expected to contribute either through lattice distortion and/or domain switching, resulting in
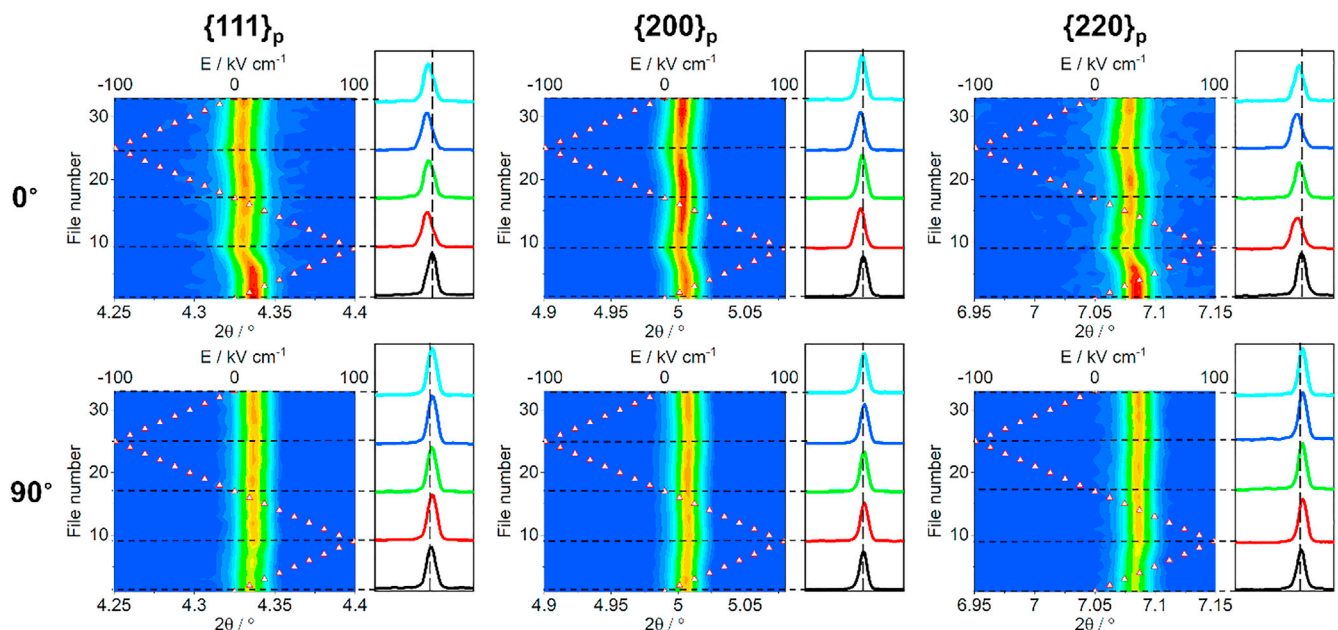

Fig. 6. Contour plots of the {111}$_p$, {200}$_p$ and {220}$_p$ peak profiles at $\psi = 0$ and 90° as a function of the variations up to maximum electric field (±100 kV cm^{-1}) obtained from the *in-situ* poling synchrotron XRD experiment for $x = 0.4$.
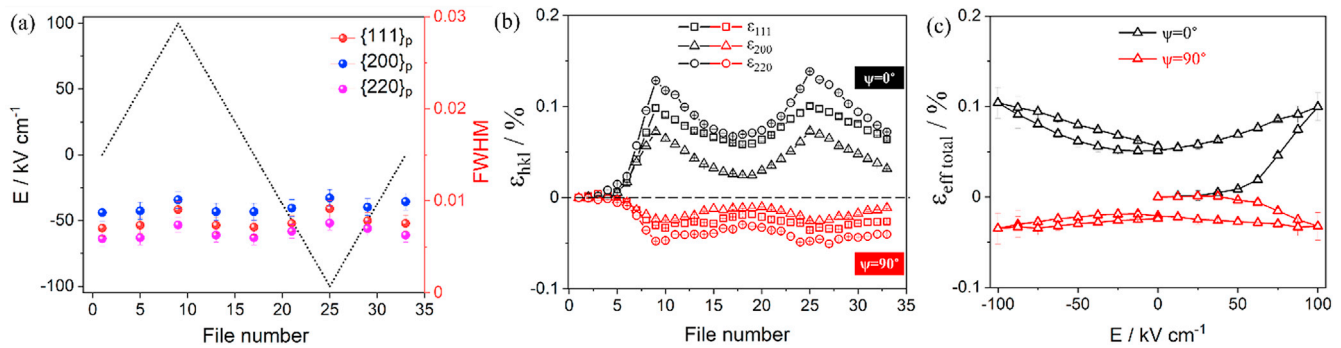
Fig. 7. (a) FWHM of the $\{111\}_p$, $\{200\}_p$ and $\{220\}_p$ peaks. (b) The ε_{111}, ε_{200} and ε_{220} for $x = 0.4$ as function of record file number with bipolar electric field up to 100 kV cm^{-1} at $\psi = 0°$ and 90°. (c) The $\varepsilon_{eff\ total}$ at $\psi = 0°$ and 90°.

splitting of the $\{111\}_p$ peak [60]. The absence of a clear contribution through splitting or widening of peaks associated with the R3c cores may be due to the relatively small volume fraction of R (15%) with respect to PC (85%) phase, giving only a negligible contribution to the peak profile. However, the absence of any change in the FWHM of the $\{111\}_p$ peak (Fig. 7a) may also suggest that the R3c cores are partially clamped by the surrounding shell matrix and do not undergo significant domain switching/distortion [11]. Some evidence of domain switching is present in the *P-E* loops (Fig. 4) but the negative strain is negligible for $x = 0.4$ and electrostriction rather than piezoelectricity is the dominant contribution to the total strain. Clamping and/or finite size effects leading to suppressing of FE behavior have been reported previously for, e.g., lead titanate ceramics as a function of grain size [61].

Given the dominant shift in $\{220\}_p$ rather than $\{111\}_p$ XRD peaks (Fig. 7b), we propose that electrostrictive behavior arises mainly from the larger PC shell volume rather than the core regions and is consistent with the "multi-symmetry polar nanoregion" model proposed by Wang and Reaney in 2019 [33]. Here, the symmetries of polar nanoregions (10−50 Å) include but are not limited to orthorhombic (O), R and T distortions. The absence of dominant R, even though the cores remain R3c, suggests that they remain inactive or insignificant due to a combination of their low volume fraction and clamping effect. The absence of any significant increase in the FWHM of the XRD peaks at 100 kV cm^{-1} suggests that any field-induced transition does not propagate throughout the grains and the coherence of distorted regions remain short-range, as reported previously in BF-BT-based compositions [11].

To further justify the "multi-symmetry polar nanoregion" model, strain orientation distribution (SOD) analysis for $x = 0.4$ on the poled remanent state ($E = 0$ kV cm^{-1}) is examined. Generally speaking, SOD refers to strain variations in the lattice as a function of ψ [40]. However, in this work, the length scale of the active polar nanoregions is nanometric and SOD refers to their strain azimuthal angle-dependence and anisotropy. The variations of ε_{hkl} as a function of ψ (the angle of the strain to the electric field) can be quantified. Azimuthal angle-dependence of representative XRD peaks of $\{111\}_p$, $\{200\}_p$ and $\{220\}_p$ at unpoled and poled states are shown in Fig. 8a and b. Individual XRD reflections at $\psi = 0°$, 30°, 60° and 90° are plotted to examine ε_{hkl} before and after poling. For the initial state (unpoled), there is no discrepancy in the peak position for four ψ values, corresponding to no apparent strain anisotropy, Fig. 8a. As shown in Fig. 6, a small irreversible change of the peak position between unpoled and poled states is induced by application of external electric field at $\psi = 0$ and 90° with peak shifts at other different ψ values also likely to occur, Fig. 8b. All three representative peaks exhibit a minor shift to higher 2θ angles with increasing ψ from 0 to 90°.

Here, the SOD (polar nanoregions) analysis at the poled remanent state is calculated from Eq. (2) using the difference on peak position between poled and unpoled states, as illustrated on (111), (200) and (220) poles in Fig. 8c. The ε_{hkl} exhibit azimuthal angle-dependence, with the highest (positive) and lowest (negative) levels of ε_{hkl} being observed at $\psi = 0°$ and 90°, respectively. The positive ε_{hkl} are found to be approximately $\varepsilon_{111} \sim +0.07\%$, $\varepsilon_{200} \sim +0.04\%$ and $\varepsilon_{220} \sim +0.08\%$ for longitudinal direction ($\psi = 0°$, centre of the pole) while the negative strains are obtained to be $\varepsilon_{111} \sim -0.03\%$, $\varepsilon_{200} \sim -0.02\%$ and $\varepsilon_{220} \sim -0.04\%$ for transverse direction ($\psi = 90°$, edge of the pole). Combining the ε_{hkl} with strain anisotropy ($\varepsilon_{220} > \varepsilon_{111} > \varepsilon_{200}$) discussed in the previous section (Fig. 7), we propose that electrostrain in BF-ST arises from a polar nanoregion model with likely, but not exclusively, O, R and T symmetries within the PC shell under applied field.

7. Conclusions

Structural and electrical performance of BF-ST electroceramics are evaluated for the first-time. Rietveld refinements confirm that, as x increases, the phase structure transforms from R to PC in (1-x) BF-xST solid solutions. Optimized electro-mechanical properties are obtained for compositions $x = 0.4$, $\varepsilon_r \sim 2500$ at ~380 °C, $P_{max} \sim 52.7$ μC cm^{-2} and $S_{max} \sim 0.15\%$. The origin of optimized electrostrain is further investigated using *in-situ* poling synchrotron XRD. For $x = 0.4$, $\{111\}_p$, $\{200\}_p$ and $\{220\}_p$ XRD reflections remain single prior, during and after application of external electric field. The absence of R3c core (represented by splitting in $\{111\}_p$ peak) in XRD maybe hidden by the complex core (small volume)-shell (large volume) microstructure. Thus, only electrostrictive (contributed from PC) but no piezoelectric response (contributed from R3c) is found during *in-situ* poling, exhibiting strain anisotropic behavior at E_{max} (100 kV cm^{-1}) and remanent states (after poling, 0 kV cm^{-1}) with $\varepsilon_{220} > \varepsilon_{111} > \varepsilon_{200}$. The optimized electrostrain behavior in a retained, averagely PC structure throughout the entire poling procedure can be only interpreted by the "multi-symmetry polar nanoregion" model, in which, presence of local short-range O, R and T distortions that cannot be probed under synchrotron XRD . Moreover, the absence of changes on FWHM even at highest electric field (100 kV cm^{-1}) suggest that any formation of local short-range distortions cannot correlate to medium- or long-range after poling. This behavior contrasts with conventional lead-based and NBT-based electrostrictors which undergo field-induced transition to a long-range FE state [62−65]. The occurrence of this unusual behavior in BF-BT and BF-ST solid solutions poses the question as to whether this is a general phenomenon across many systems or restricted uniquely to compositions derived from BF.
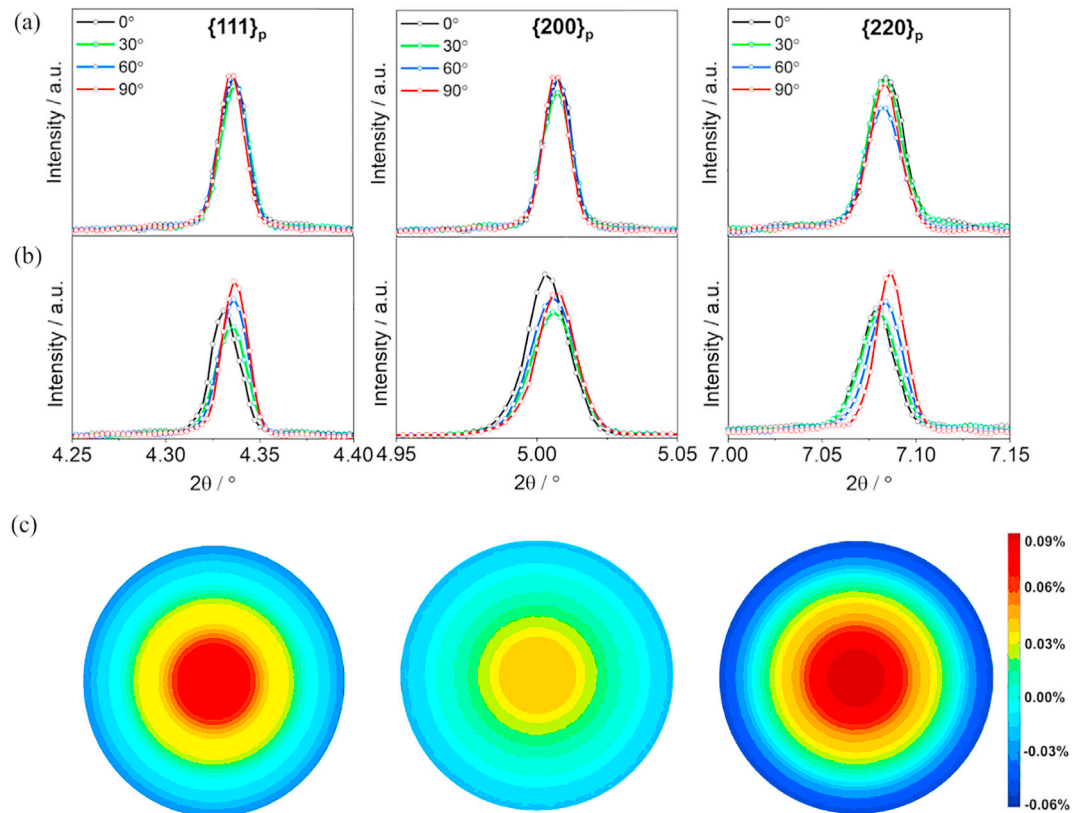
Fig. 8. Azimuthal angle-dependence of three representative peaks of {111}$_p$, {200}$_p$ and {220}$_p$ for (a) unpoled, (b) poled $x = 0.4$ ceramics and (c) ε_{hkl} for (111), (200) and (220) poles.

CRediT author statement

Dawei Wang and Ian M. Reaney supervised the project, Zhilun Lu wrote the article, carried out all property measuremnts and contributed to all microstructure charaterizations, Zhilun Lu, Ge Wang, Linhao Li, Dawei Wang and Annette K. Kleppe contributed to the in-situ synchrotron X-ray experiment. Ge Wang and Zhilun Lu contributed to the corresponding data analysis, Weichao Bao and Fangfang Xu conducted the transmission electron microscopy characterizations, Antonio Feteira and Yuhe Huang contributed to data discussion, All the authors discussed the results and commented on the manuscript.

Declaration of competing interest

The authors declare that they have no known competing financial interests or personal relationships that could have appeared to influence the work reported in this paper.

Acknowledgements

References

[1] J.B. Neaton, C. Ederer, U.V. Waghmare, N.A. Spaldin, K.M. Rabe, First-principles study of spontaneous polarization in multiferroic BiFeO$_3$, Phys. Rev. B 71 (2005): 014113.

[2] D. Lebeugle, D. Colson, A. Forget, M. Viret, Very large spontaneous electric polarization in BiFeO$_3$ single crystals at room temperature and its evolution under cycling fields, Appl. Phys. Lett. 91 (2007): 022907.

[3] D.I. Woodward, I.M. Reaney, R.E. Eitel, C.A. Randall, Crystal and domain structure of the BiFeO$_3$-PbTiO$_3$ solid solution, J. Appl. Phys. 94 (2003) 3313−3318.

[4] Y. Ma, X.M. Chen, Enhanced multiferroic characteristics in NaNbO$_3$-modified BiFeO$_3$ ceramics, J. Appl. Phys. 105 (2009): 054107.

[5] V. Dorcet, P. Marchet, G. Trolliard, Structural and dielectric studies of the Na$_{0.5}$Bi$_{0.5}$TiO$_3$-BiFeO$_3$ system, J. Eur. Ceram. Soc. 27 (2007) 4371−4374.

[6] H. Liu, X. Yang, Structural, dielectric, and magnetic properties of BiFeO$_3$-SrTiO$_3$ solid solution ceramics, Ferroelectrics 500 (2016) 310−317.

[7] Y.F. Hou, W.L. Li, T.D. Zhang, W. Wang, W.P. Cao, X.L. Liu, W.D. Fei, Large piezoelectric response of BiFeO$_3$/BaTiO$_3$ polycrystalline films induced by the low-symmetry phase, Phys. Chem. Chem. Phys. 17 (2015) 11593−11597.

[8] T. Zheng, J. Wu, Perovskite BiFeO$_3$-BaTiO$_3$ Ferroelectrics: engineering properties by domain evolution and thermal depolarization modifcation, Adv. Electron. Mater. 6 (2020) 2000079.

[9] J. Rödel, W. Jo, K.T.P. Seifert, E.-M. Anton, T. Granzow, D. Damjanovic, Perspective on the development of lead-free piezoceramics, J. Am. Ceram. Soc. 92 (2009) 1153−1177.

[10] J. Chen, J. Cheng, J. Guo, Z. Cheng, J. Wang, H. Liu, S. Zhang, Excellent thermal stability and aging behaviors in BiFeO$_3$-BaTiO$_3$ piezoelectric ceramics with rhombohedral phase, J. Am. Ceram. Soc. 103 (2019) 374−381.

[11] I. Calisir, A.K. Kleppe, A. Feteira, D.A. Hall, Quenching-assisted actuation mechanisms in core-shell structured BiFeO$_3$-BaTiO$_3$ piezoceramics, J. Mater. Chem. C 7 (2019) 10218−10230.

[12] T. Rojac, A. Bencan, B. Malic, G. Tutuncu, J.L. Jones, J.E. Daniels, D. Damjanovic, D.J. Green, BiFeO$_3$ ceramics: processing, electrical, and electromechanical properties, J. Am. Ceram. Soc. 97 (2014) 1993−2011.

[13] D. Wang, G. Wang, S. Murakami, Z. Fan, A. Feteira, D. Zhou, S. Sun, Q. Zhao, I.M. Reaney, BiFeO$_3$-BaTiO$_3$: a new generation of lead-free electroceramics, J. Adv. Dielectr. 8 (2019) 1830004.

[14] Q. Zheng, L. Luo, K.H. Lam, N. Jiang, Y. Guo, D. Lin, Enhanced ferroelectricity, piezoelectricity, and ferromagnetism in Nd-modified BiFeO$_3$-BaTiO$_3$ lead-free ceramics, J. Appl. Phys. 116 (2014) 184101.

[15] X. Wu, M. Tian, Y. Guo, Q. Zheng, L. Luo, D. Lin, Phase transition, dielectric, ferroelectric and ferromagnetic properties of La-doped BiFeO$_3$-BaTiO$_3$ multi-ferroic ceramics, J. Mater. Sci. Mater. Electron. 26 (2014) 978−984.

[16] D. Wang, A. Khesro, S. Murakami, A. Feteira, Q. Zhao, I.M. Reaney, Temperature dependent, large electromechanical strain in Nd-doped BiFeO$_3$-BaTiO$_3$ lead-free ceramics, J. Eur. Ceram. Soc. 37 (2017) 1857−1860.

[17] Q. Zhou, C. Zhou, H. Yang, G. Chen, W. Li, H. Wang, S. Zhang, Dielectric, ferroelectric, and piezoelectric properties of Bi(Ni$_{1/2}$Ti$_{1/2}$)O$_3$-modified BiFeO$_3$-BaTiO$_3$ ceramics with high curie temperature, J. Am. Ceram. Soc. 95 (2012) 3889−3893.

[18] T. Zheng, J. Wu, Effects of site engineering and doped element types on piezoelectric and dielectric properties of bismuth ferrite lead-free ceramics, J. Mater. Chem. C 3 (2015) 11326−11334.

[19] I. Fujii, R. Iizuka, Y. Nakahira, Y. Sunada, S. Ueno, K. Nakashima, E. Magome, C. Moriyoshi, Y. Kuroiwa, S. Wada, Electric field induced lattice strain in pseudocubic Bi(Mg$_{1/2}$Ti$_{1/2}$)O$_3$-modified BaTiO$_3$-BiFeO$_3$ piezoelectric ceramics, Appl. Phys. Lett. 108 (2016) 172903.

[20] S.A. Khan, F. Akram, I. Bae, T. Ahmed, T.K. Song, Y.S. Sung, M.-H. Kim, S. Lee, Enhancing piezoelectric coefficient with high Curie temperature in BiAlO$_3$-modified BiFeO$_3$-BaTiO$_3$ lead-free ceramics, Solid State Sci. 98 (2019) 106040.

[21] S. Murakami, N.T.A.F. Ahmed, D. Wang, A. Feteira, D.C. Sinclair, I.M. Reaney, Optimising dopants and properties in BiMeO$_3$ (Me = Al, Ga, Sc, Y, Mg$_{2/3}$Nb$_{1/3}$, Zn$_{2/3}$Nb$_{1/3}$, Zn$_{1/2}$Ti$_{1/2}$) lead-free BaTiO$_3$-BiFeO$_3$ based ceramics for actuator applications, J. Eur. Ceram. Soc. 38 (2018) 4220−4231.

[22] C. Zhou, Z. Cen, H. Yang, Q. Zhou, W. Li, C. Yuan, H. Wang, Structure, electrical properties of Bi(Fe, Co)O$_3$-BaTiO$_3$ piezoelectric ceramics with improved Curie temperature, Phys. B Condens. Matter 410 (2013) 13−16.

[23] W. Zhou, Q. Zheng, Y. Li, Q. Li, Y. Wan, M. Wu, D. Lin, Structure, ferroelectric, ferromagnetic, and piezoelectric properties of Al-modified BiFeO$_3$-BaTiO$_3$ multiferroic ceramics, Phys. Status Solidi 212 (2015) 632−639.

[24] X.-H. Liu, Z. Xu, S.-B. Qu, X.-Y. Wei, J.-L. Chen, Ferroelectric and ferromagnetic properties of Mn-doped 0.7BiFeO$_3$-0.3BaTiO$_3$ solid solution, Ceram. Int. 34 (2008) 797−801.

[25] Y. Wan, Y. Li, Q. Li, W. Zhou, Q. Zheng, X. Wu, C. Xu, B. Zhu, D. Lin, J. Jones, Microstructure, ferroelectric, piezoelectric, and ferromagnetic properties of Sc-modified BiFeO$_3$-BaTiO$_3$ multiferroic ceramics with MnO$_2$ addition, J. Am. Ceram. Soc. 97 (2014) 1809−1818.

[26] I. Fujii, R. Mitsui, K. Nakashima, N. Kumada, M. Shimada, T. Watanabe, J. Hayashi, H. Yabuta, M. Kubota, T. Fukui, S. Wada, Structural, dielectric, and piezoelectric properties of Mn-Doped BaTiO$_3$-Bi(Mg$_{1/2}$Ti$_{1/2}$)O$_3$-BiFeO$_3$ ceramics, Jpn. J. Appl. Phys. 50 (2011): 09nd07.

[27] X. Wu, L. Luo, N.A. Jiang, X. Wu, Q. Zheng, Effects of Nb doping on the microstructure, ferroelectric and piezoelectric properties of 0.7BiFeO$_3$-0.3BaTiO$_3$ lead-free ceramics, Bull. Mater. Sci. 39 (2016) 737−742.

[28] Y.-K. Jun, W.-T. Moon, C.-M. Chang, H.-S. Kim, H.S. Ryu, J.W. Kim, K.H. Kim, S.-H. Hong, Effects of Nb-doping on electric and magnetic properties in multi-ferroic BiFeO$_3$ ceramics, Solid State Commun. 135 (2005) 133−137.

[29] Q. Fan, C. Zhou, W. Zeng, L. Cao, C. Yuan, G. Rao, X. Li, Normal-to-relaxor ferroelectric phase transition and electrical properties in Nb-modified 0.72BiFeO$_3$-0.28BaTiO$_3$ ceramics, J. Electroceram. 36 (2015) 1−7.

[30] S. Murakami, D. Wang, A. Mostaed, A. Khesro, A. Feteira, D.C. Sinclair, Z. Fan, X. Tan, I.M. Reaney, High strain (0.4%) Bi(Mg$_{2/3}$Nb$_{1/3}$)O$_3$-BaTiO$_3$-BiFeO$_3$ lead-free piezoelectric ceramics and multilayers, J. Am. Ceram. Soc. 101 (2018) 5428−5442.

[31] J. Chen, J.E. Daniels, J. Jian, Z. Cheng, J. Cheng, J. Wang, Q. Gu, S. Zhang, Origin of large electric-field-induced strain in pseudo-cubic BiFeO$_3$-BaTiO$_3$ ceramics, Acta Mater. 197 (2020) 1−9.

[32] Y. Kuroiwa, S. Kim, I. Fujii, S. Ueno, Y. Nakahira, C. Moriyoshi, Y. Sato, S. Wada, Piezoelectricity in perovskite-type pseudo-cubic ferroelectrics by partial ordering of off-centered cations, Commun. Mater. 1 (2020) 1−8.

[33] G. Wang, Z. Fan, S. Murakami, Z. Lu, D.A. Hall, D.C. Sinclair, A. Feteira, X. Tan, J.L. Jones, A.K. Kleppe, D. Wang, I.M. Reaney, Origin of the large electrostrain in BiFeO$_3$-BaTiO$_3$ based lead-free ceramics, J. Mater. Chem. 7 (2019) 21254−21263.

[34] I. Calisir, A.A. Amirov, A.K. Kleppe, D.A. Hall, Optimisation of functional properties in lead-free BiFeO$_3$-BaTiO$_3$ ceramics through La^{3+} substitution strategy, J. Mater. Chem. 6 (2018) 5378−5397.

[35] Y. Li, Y. Chen, Z. Zhang, A. Kleppe, D.A. Hall, In-situ XRD study of actuation mechanisms in BiFeO$_3$-K$_{0.5}$Bi$_{0.5}$TiO$_3$-PbTiO$_3$ ceramics, Acta Mater. 168 (2019) 411−425.

[36] Y. Li, Z. Zhang, Y. Chen, D.A. Hall, Electric field-induced strain in core-shell structured BiFeO$_3$-K$_{0.5}$Bi$_{0.5}$TiO$_3$-PbTiO$_3$ ceramics, Acta Mater. 160 (2018) 199−210.

[37] J.E. Daniels, W. Jo, J. Rödel, J.L. Jones, Electric-field-induced phase trans-formation at a lead-free morphotropic phase boundary: case study in a 93%(Bi$_{0.5}$Na$_{0.5}$)TiO$_3$-7% BaTiO$_3$ piezoelectric ceramic, Appl. Phys. Lett. 95 (2009): 032904.

[38] W. Jo, J.E. Daniels, J.L. Jones, X. Tan, P.A. Thomas, D. Damjanovic, J. Rödel, Evolving morphotropic phase boundary in lead-free (Bi$_{1/2}$Na$_{1/2}$)TiO$_3$-BaTiO$_3$ piezoceramics, J. Appl. Phys. 109 (2011): 014110.

[39] R.D.W. Jo, M. Acosta, J. Zang, C. Groh, E. Sapper, K. Wang, J. Rödel, Giant electric-field-induced strains in lead-free ceramics for actuator applications − status and perspective, J. Electroceram. 29 (2012) 71−93.

[40] S. Zhang, A.B. Kounga, E. Aulbach, H. Ehrenberg, J. Rödel, Giant strain in lead-free piezoceramics Bi$_{0.5}$Na$_{0.5}$-BaTiO$_3$-K$_{0.5}$Na$_{0.5}$NbO$_3$ system, Appl. Phys. Lett. 91 (2007) 112906.

[41] J. Kling, X. Tan, W. Jo, H.-J. Kleebe, H. Fuess, J. Rödel, In situ transmission electron microscopy of electric field-triggered reversible domain formation in Bi-based lead-free piezoceramics, J. Am. Ceram. Soc. 93 (2010) 2452−2455.

[42] W. Zheng, L. Zhang, Y. Lin, Z. Shi, F. Cao, G. Yuan, J. Yu, Ferroic phase transi-tions and switching properties of modified BiFeO$_3$-SrTiO$_3$ multiferroic pe-rovskites, J. Mater. Sci. Mater. Electron. 27 (2016) 12067−12073.

[43] A. Kumar, A. Kumar, S. Saha, H. Basumatary, R. Ranjan, Ferromagnetism in the multiferroic alloy systems BiFeO$_3$-BaTiO$_3$ and BiFeO$_3$-SrTiO3: intrinsic or extrinsic, Appl. Phys. Lett. 114 (2019): 022902.

[44] S. Vura, P.S. Anil Kumar, A. Senyshyn, R. Ranjan, Magneto-structural study of the multiferroic BiFeO$_3$-SrTiO$_3$, J. Magn. Magn Mater. 365 (2014) 76−82.

[45] R. Ranjith, B. Kundys, W. Prellier, Periodicity dependence of the ferroelectric properties in BiFeO$_3$∕SrTiO$_3$ multiferroic superlattices, Appl. Phys. Lett. 91 (2007) 222904.

[46] Z. Lu, G. Wang, W. Bao, J. Li, L. Li, A. Mostaed, H. Yang, H. Ji, D. Li, A. Feteira, F. Xu, D.C. Sinclair, D. Wang, S.-Y. Liu, I.M. Reaney, Superior energy density through tailored dopant strategies in multilayer ceramic capacitors, Energy Environ. Sci. 13 (2020) 2938−2948.

[47] Z.Z. Ma, Z.M. Tian, J.Q. Li, C.H. Wang, S.X. Huo, H.N. Duan, S.L. Yuan, Enhanced polarization and magnetization in multiferroic (1-x)BiFeO$_3$-xSrTiO$_3$ solid so-lution, Solid State Sci. 13 (2011) 2196−2200.

[48] J. Wei, D. Fu, J. Cheng, J. Chen, Temperature dependence of the dielectric and piezoelectric properties of xBiFeO$_3$-(1-x)BaTiO$_3$ ceramics near the morpho-tropic phase boundary, J. Mater. Sci. 52 (2017) 10726−10737.

[49] M. Makarovic, A. Bencan, J. Walker, B. Malic, T. Rojac, Processing, piezoelectric and ferroelectric properties of (x)BiFeO$_3$-(1-x)SrTiO$_3$ ceramics, J. Eur. Ceram. Soc. 39 (2019) 3693−3702.

[50] T.H. Wang, C.S. Tu, Y. Ding, T.C. Lin, C.S. Ku, W.C. Yang, H.H. Yu, K.T. Wu, Y.D. Yao, H.Y. Lee, Phase transition and ferroelectric properties of xBiFeO$_3$-(1-x)BaTiO$_3$ ceramics, Curr. Appl. Phys. 11 (2011) S240−S243.

[51] V. Kovacova, N. Vaxelaire, G. Le Rhun, P. Gergaud, T. Schmitz-Kempen, E. Defay, Correlation between electric-field-induced phase transition and piezoelectricity in lead zirconate titanate films, Phys. Rev. B 90 (2014) 140101.

[52] M. Otonicar, J. Park, M. Logar, G. Esteves, J.L. Jones, B. Jancar, External-field-induced crystal structure and domain texture in (1-x)Na$_{0.5}$Bi$_{0.5}$TiO$_3$-xK$_{0.5}$Bi$_{0.5}$TiO$_3$ piezoceramics, Acta Mater. 127 (2017) 319−331.

[53] J.E. Daniels, W. Jo, J. Rödel, V. Honkimäki, J.L. Jones, Electric-field-induced phase-change behavior in (Bi$_{0.5}$Na$_{0.5}$)TiO$_3$-BaTiO$_3$-(K$_{0.5}$Na$_{0.5}$)NbO$_3$: a combi-natorial investigation, Acta Mater. 58 (6) (2010) 2103−2111.

[54] J.L. Jones, B.J. Iverson, K.J. Bowman, Texture and anisotropy of polycrystalline piezoelectrics, J. Am. Ceram. Soc. 90 (2007) 2297−2314.

[55] J.C.H. Liu, H. Huang, L. Fan, Y. Ren, Z. Pan, J. Deng, L. Chen, X. Xing, Role of reversible phase transformation for strong piezoelectric performance at the morphotropic phase boundary, Phys. Rev. Lett. 120 (2018): 055501.

[56] J.C.H. Liu, L. Fan, Y. Ren, Z. Pan, K.V. Lalitha, J. Rödel, X. Xing, Critical role of monoclinic polarization rotation in high-performance perovskite piezoelectric materials, Phys. Rev. Lett. 119 (2017): 017601.

[57] M.R. Daymond, The determination of a continuum mechanics equivalent elastic strain from the analysis of multiple diffraction peaks, J. Appl. Phys. 96 (2004) 4263−4272.

[58] L. Daniel, D.A. Hall, J. Koruza, K.G. Webber, A. King, P.J. Withers, Revisiting the blocking force test on ferroelectric ceramics using high energy x-ray diffrac-tion, J. Appl. Phys. 117 (2015) 174104.

[59] R.D. Shannon, Revised effective ionic radii and systematic studies of inter-atomic distances in halides and chalcogenides, Acta Crystallogr. A32 (1976) 751−767.

[60] G. Wang, Z. Lu, Z. Zhang, A. Feteira, C.C. Tang, D.A. Hall, Electric field-induced irreversible relaxor to ferroelectric phase transformations in Na$_{0.5}$Bi$_{0.5}$TiO$_3$-NaNbO$_3$ ceramics, J. Am. Ceram. Soc. 102 (2019) 7746−7754.

[61] P. Sooksaen, I.M. Reaney, D.C. Sinclair, Engineered sintering aids for PbO-based electroceramics, J. Electroceram. 18 (2007) 77−85.

[62] H. Liu, L. Fan, S. Sun, K. Lin, Y. Ren, X. Tan, X. Xing, J. Chen, Electric-field-induced structure and domain texture evolution in PbZrO$_3$-based antiferro-electric by in-situ high-energy synchrotron X-ray diffraction, Acta Mater. 184 (2020) 41−49.

[63] L. Zhang, J. Chen, L. Fan, O. Diéguez, J. Cao, Z. Pan, Y. Wang, J. Wang, M. Kim, S. Deng, J. Wang, H. Wang, J. Deng, R. Yu, J.F. Scott, X. Xing, Giant polarization in super-tetragonal thin films through interphase strain, Science 361 (2018) 494−497.

[64] Ge Wang, Zhilun AntonGoetzee-BarralLu, Dean S.Keeble, David A Hall, Thermally-induced local structural transformations in Na$_{0.5}$Bi$_{0.5}$TiO$_3$-KNbO$_3$ ceramics, J. Eur. Ceram. Soc. 41 (2021) 3832−3837.

[65] Ge Wang, David A. Hall, Yizhe Li, A. ClaireMurray, C. ChiuTang, Structural characterization of the electric field-induced ferroelectric phase in Na$_{0.5}$Bi$_{0.5}$TiO$_3$-KNbO$_3$ ceramics, J. Eur. Ceram. Soc. 36 (2016) 4015−4021.